# Toward characterization of the aerosol optical properties over Loess Plateau of Northwestern China

Jianrong Bi [a], Jianping Huang [a,*], Qiang Fu [a,b], Xin Wang [a], Jinsen Shi [a], Wu Zhang [a], Zhongwei Huang [a], Beidou Zhang [a]

[a] Key Laboratory for Semi-Arid Climate Change of the Ministry of Education, College of Atmospheric Sciences, Lanzhou University, Lanzhou 730000, PR China
[b] Department of Atmospheric Sciences, University of Washington, Seattle, WA 98105, USA

## ARTICLE INFO

## ABSTRACT

Aerosol optical properties were obtained from a CIMEL sunphotometer of the Aerosol Robotic Network at the Semi-Arid Climate and Environment Observatory of Lanzhou University (SACOL). SACOL is located over the Loess Plateau of the Northwestern China. The observed data are analyzed for the period of August 2006–October 2008. We find that aerosol optical depths (AODs) have a pronounced annual cycle, with a maximum dust aerosol loading during the spring. The 2-year average values of AOD, Ångström exponent ($\alpha$), and water vapor path (WVP) along with their standard deviation (in parenthesis) are 0.35 (0.21), 0.93 (0.34), and 0.77 cm (0.52 cm), respectively. The probability distributions of these quantities all have one modal value, which are 0.3, 1.1, and 0.5 cm, respectively. There is a notable feature in the relationship between daily averaged AOD and Ångström exponent: a wide range of $\alpha$ corresponding to moderate to low aerosol optical depths ($< 0.8$). There is no significant correlation between daily averaged WVP and AOD. However the daily averaged Ångström exponent and WVP show a significant positive correlation, indicating that the smaller aerosol particles present when the WVP is large. Variations of the retrieved aerosol volume size distributions are mainly associated with the changes in the concentration of the coarse aerosol fraction. The geometric mean radii for the fine and coarse aerosols are 0.18 $\mu$m ($\pm 0.03 \mu$m), and 2.53 $\mu$m ($\pm 0.25 \mu$m), respectively. The spectral dependences of the single scattering albedos are different between the dusty and non-dusty conditions. In the presence of dust, the SSAs increase slightly with wavelength. When dust is not a major component, the corresponding values decrease with wavelength.

© 2010 Elsevier Ltd. All rights reserved.

## 1. Introduction

Aerosol particles, as important constituents of the earth atmosphere, play an important role in the global and regional climate by scattering and absorbing solar radiation [1–6]. Mineral dust is a major part of natural aerosols in the atmosphere [7], and has a great effect on the radiation budget and hydrologic cycle of the Earth's system [8,9].

Mineral dust can also cause changes in cloud properties, such as the number concentration and size of cloud droplets, which can alter both cloud albedo and cloud lifetime [5,10]. However, these dust radiative forcing and their climatic effects still contain considerable uncertainties due to the lack of understanding to aerosol properties and their spatial and temporal distributions [11].

East Asia is one of the major source regions of mineral dust aerosols in the world [12,13]. Every year, deserts in Eastern Asia produce a large amount of mineral dust particles that become entrained in the atmosphere [14]. They can be transported over thousands of kilometers by

the westerlies [15–17]. Fully accounting for aerosol effects on climate requires extensive measurements of aerosol optical, microphysical and chemical properties, and their spatial and temporal distributions.

In recent years, many investigations and field experiments have focused on the optical properties of dust aerosols in the East Asian region surrounding China [4,12,18–22]. These studies are vital to understand the characteristics and variations of dust aerosols in East Asian so that we can evaluate more accurately the effect of mineral dust aerosols on global and regional climate change in the future. However, there have been very few studies examining the atmospheric aerosol properties over Northwestern China where is a major source region of dust aerosols.

This work is mainly to examine the aerosol optical properties obtained at the Semi-Arid Climate and Environment Observatory of Lanzhou University (SACOL) which is located over the Loess Plateau of Northwestern China (see Fig. 1). We investigate seasonal and inter-annual variabilities of aerosol optical depth and its spectral behavior. We also present the characteristics of volume size distribution, single scattering albedo, asymmetry parameter, and complex refractive index as well.

## 2. Site and measurements

An automatic sun and sky scanning radiometer (CIMEL Sunphotometer) was set up at SACOL (latitude: 35.946° N, longitude: 104.133°E, and elevation: 1970 m) from August 2006. It is one of the Aerosol Robotic Network (AERONET) sites over Loess Plateau in Northwestern China. SACOL is a rural site and located on the top of Tsuiying Mountain, which is about 50 km southeast of Lanzhou city at the southern bank of Yellow River [22]. In addition, this site is situated at the south edge of the Tengger Desert, which is a typical dust activity center in Northwest China (Fig. 1).

The detailed descriptions of the instrument and data acquisition procedures were given by Huang et al. [22].

The CIMEL sun/sky radiometer makes measurements of the direct sun and diffuse sky radiances within the spectral range 340–1020 nm [23]. The automatic tracking sun and sky scanning radiometer makes direct sun measurements with a 1.2 full field of view at every 15 min in eight spectral channels at 340, 380, 440, 500, 675, 870, 940, and 1020 nm (nominal wavelengths). Seven of the eight bands are used to acquire aerosol optical depth data. The eighth band at 940 nm is used to retrieve total precipitable water content in centimeters. The instrument's calibration is carried out at the pristine Mauna Loa Observatory (MLO; latitude: 19°53′N, longitude: 15 5°57′W, elevation: 3400 m) once per year. The calibration coefficients of aerosol optical depth measurements were based on an intercomparsion with a reference instrument that was calibrated using Langley plots from data collected. Radiance measurements were calibrated using a two meters integrating sphere at NASA Goddard Space Flight Center [23].

Holben et al. [23] and Eck et al. [24] presented that the total uncertainty in aerosol optical depth (AOD) for a field instrument is about 0.01–0.02. The details of water vapor path (WVP) retrieval procedure and errors involved can be found in [25]. The retrieved precipitable water vapor path is consistent with radiosonde and microwave radiometer measurements within ~10%. The accuracy of the aerosol particle size distributions and single scattering albedos has been studied in detail by [26]. Retrieval errors in $dV/d \ln R$ typically do not exceed 15–35% (depending on aerosol type) for each particle radius bin within the 0.1–7 μm range. The errors for very small particles ($r \sim 0.05$–0.1 μm) and very large particle ($r \sim 7$–15 μm) may be as large as 35–100% for given particle radius bin. However, no significant shifts in the positions of mode radii or changes in the shape of size distributions are expected. Single
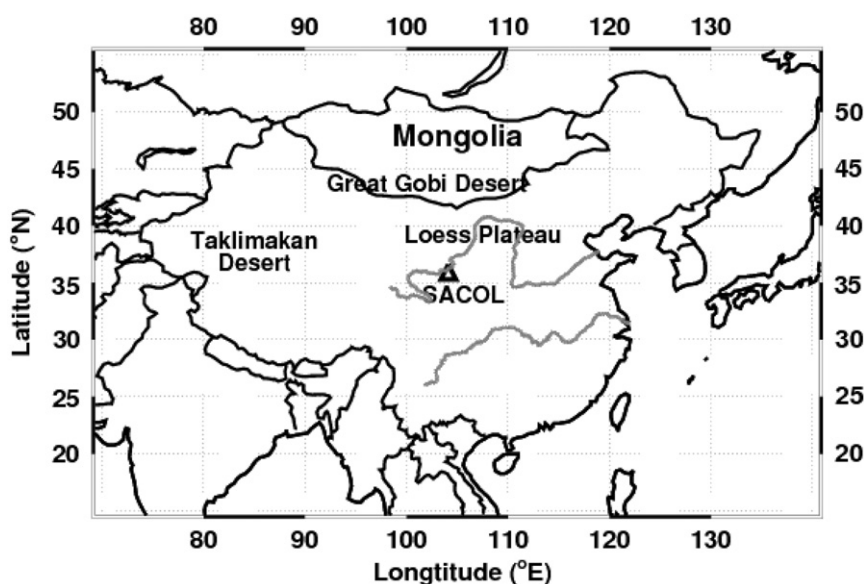


**Fig. 1.** Location of the SACOL observatory over China.

scattering albedos are expected to have an uncertainty of 0.03–0.05 depending on aerosol type and loading [27].

The data sets used in this article come from the Level 2.0 quality-assured data of the AERONET (http://aeronet. gsfc.nasa.gov). They are pre- and post-field calibrated, automatically cloud screened [28], and manually inspected. There are two sun photometers at SACOL. When one instrument was sent to the Goddard Space Flight Center (GSFC) for the calibration, the backup instrument operates continuously.

## 3. Results

### 3.1. Variability of aerosol optical properties and water vapor path

The aerosol optical properties are characterized by two important parameters: the aerosol optical depth at 500 nm wavelength, $\tau_a$ (500 nm), and the Ångström exponent, $\alpha$. The $\alpha$ is derived from a multispectral log linear fit to $\tau_a \sim \lambda^{-\alpha}$ based on four wavelengths in the range 440–870 nm. Although not all optical depth spectra are well represented by an Ångström exponent fit (e.g., [24,29–31]), the Ångström exponent $\alpha$ can still be considered as a first-order indicator of the average spectral behavior.

Fig. 2a shows the monthly average aerosol optical depth at 500 nm for about 2 year record (August 2006–October 2008) at SACOL based on a total of 552 daily averaged data. The maximum monthly mean value appears in January 2008, which is ~0.60($\pm$0.34). The minimum mean value occurs in September 2008 which is 0.20($\pm$0.078). There is a distinct annual pattern with an increase to maximum turbidity in the springtime for all the years. A summer–autumn minimum is always in evidence. The monthly mean aerosol optical depth increases from autumn to a peak in springtine and decreases back to minimum value by summer–autumn. The mean value of $\tau_a$ (500 nm) in January 2008 is 0.60. In contrast, the mean aerosol optical depth between the months of June and September decreases to a minimum of about ~0.20 in September 2008. Standard deviations generally increase with the mean values of $\tau_a$. Monthly averages of the Ångström exponent $\alpha$ for the whole period of observations are shown in Fig. 2b. The notable decrease of the Ångström exponent (Fig. 2b) during the March–May in both years is associated with the presence of dust in the aerosol loading. The monthly mean values of the Ångström exponent vary from 0.4 to 1.3, showing a March–April minimum. The monthly average values of the WVP also vary remarkably. The minimum mean value of WVP in wintertime is ~0.2 cm. It increases gradually from January to August, with a maximum value of more than ~1.6 cm. The later is mainly associated with the presence of rainy season during the summer–autumn seasons.

The daily average values of $\tau_a$ (500 nm) do show very large day-to-day variations, especially during the spring-time (Fig. 3a). The annual pattern with an increase to maximal turbidity in the February to May period is apparent. The July–October minimum is also in evidence
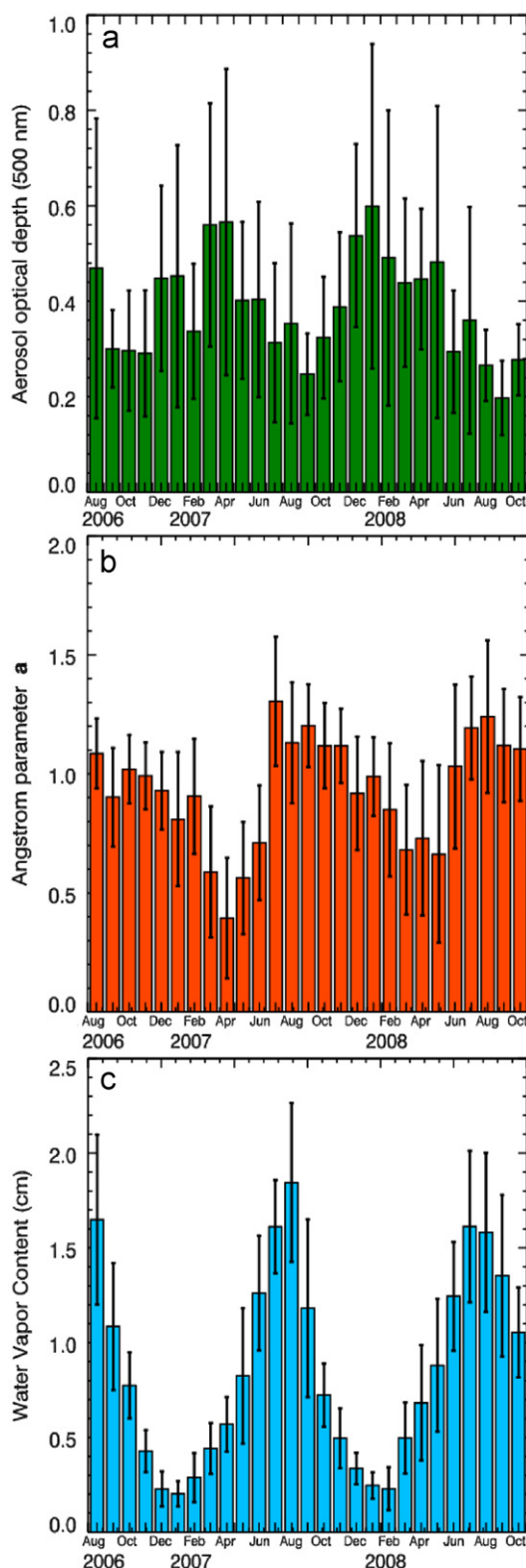


**Fig. 2.** Mean monthly values of (a) aerosol optical depth at the 500 nm wavelength, (b) Ångström parameter, and (c) water vapor path for the whole period of measurements (the bars indicate plus or minus one standard deviation).
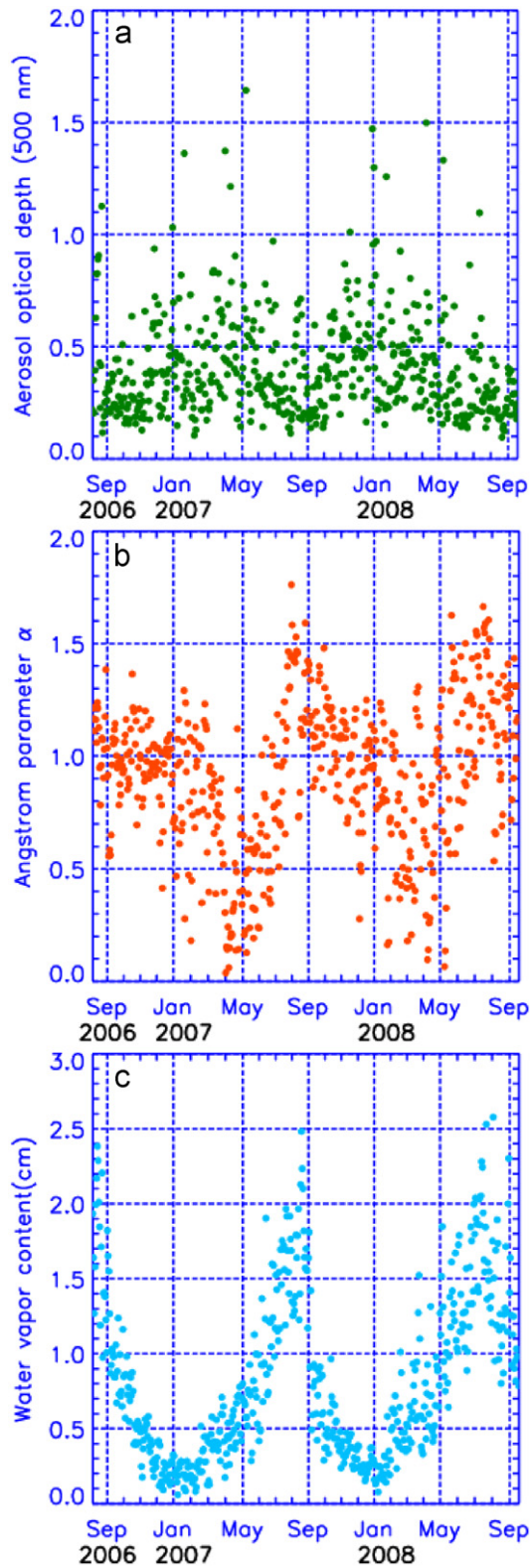
**Fig. 3.** Mean daily values of (a) aerosol optical depth at the 500 nm wavelength, (b) Ångström exponent, and (c) water vapor path for the whole period of measurements.
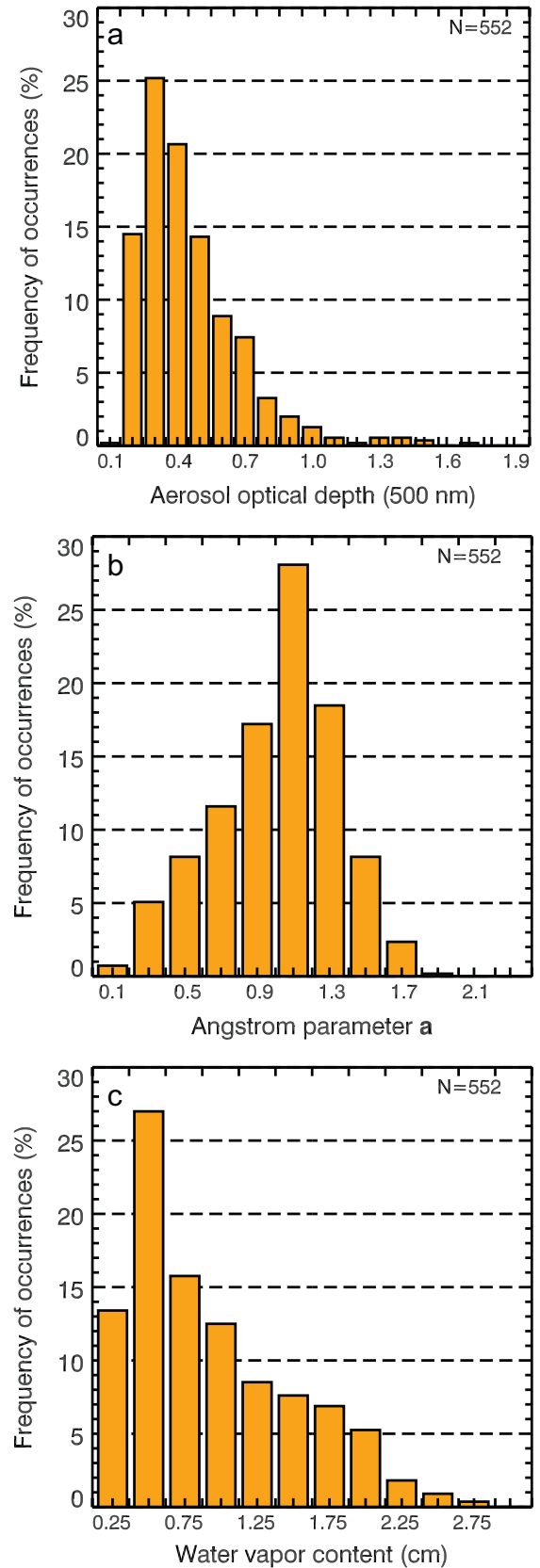


**Fig. 4.** Frequency of occurrences of (a) aerosol optical depth at the 500 nm wavelength, (b) Ångström exponent, and (c) water vapor path.

and daily average $\tau_a$ (500 nm) drops to about 0.10 on a few occasions in this period. High daily average values of the Ångström exponent $\alpha$ from July to October for the whole period reflect the presence of a significant fraction of fine particles in the aerosol size distribution. The origin of this aerosol is, most likely, local or regional anthropogenic pollutants. Dusty conditions prevailed starting in March and $\alpha$ usually remained below unity in the spring. The daily average WVPs (Fig. 3c) show high values with a range 1.0–2.6 cm in the summertime, while in November–June they are usually less than 1.0 cm. This is consistent with the general synoptic pattern for this region, which are cold and dry in winter and moist and warm in summer. The interannual variability of precipitable water is also quite apparent from year to year.

Frequency histograms of $\tau_a$, $\alpha$, and WVP are shown in Fig. 4a–c using the daily averaged data. The aerosol optical depth probability distribution has a modal value of $\sim$0.3, varying within 0.1–1.7 range. The probability distribution of $\alpha$ has a modal value of $\sim$1.1, and ranges from 0 to 1.7. The frequency histogram of WVP shows a maximum at 0.5 cm, varies within 0.25–2.75 cm range.

The seasonal dependences of the frequency histograms of $\tau_a$, $\alpha$, and WVP values are presented in Fig. 5. The

autumn season has the narrowest $\tau_a$ probability distribution with the modal value of 0.3. The distribution in summer season is wider and also with one modal value of 0.3. The distributions of the spring and winter seasons are the widest, vary between 0.2–1.7 and 0.2–1.5, respectively. These two seasons both have a modal $\tau_a$ value of about 0.4. Note that the 2-year averaged aerosol optical depth is 0.35 and seasonal mean values are 0.415($\pm$0.23), 0.291($\pm$0.186), 0.283($\pm$0.135), and 0.426($\pm$0.217) for spring, summer, autumn, and winter, respectively. The largest daily averaged value of AOD is found in springtime due to the dust weather events.

A parallel set of the Ångström exponent plots in Fig. 5 also displays an obvious seasonal variation. In autumn season the $\alpha$ distribution is rather narrow and peaks around $\alpha\sim$1.1, varying in 0.7–1.5 range. The probability distribution in winter season is also narrow and with a modal value of 1.1. In the spring season dusty conditions prevail and the maximum of the distribution shifts toward a smaller $\alpha$ near $\sim$0.7. The broad summer season distribution characterizes more complex conditions, when dust is also present; however, non-dust conditions occur relatively more often.

Note that the 2-year mean value of Ångström exponent is 0.93($\pm$0.34), and seasonal means are 0.649($\pm$0.316),
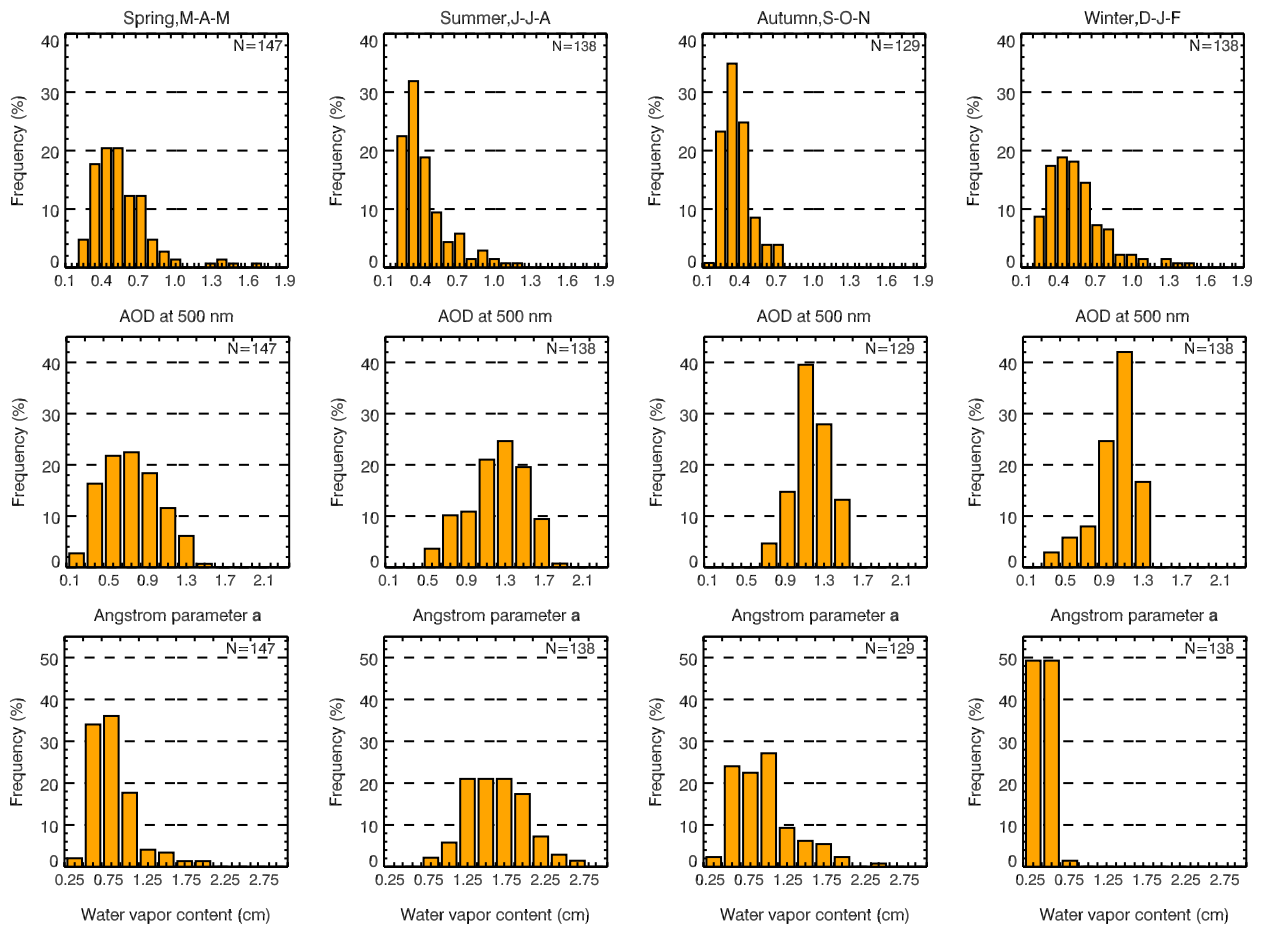


**Fig. 5.** Seasonal frequency of occurrences of aerosol optical depth at the 500 nm wavelength, Ångström exponent, and water vapor path. The sum of frequencies is equal to 100% for each season.
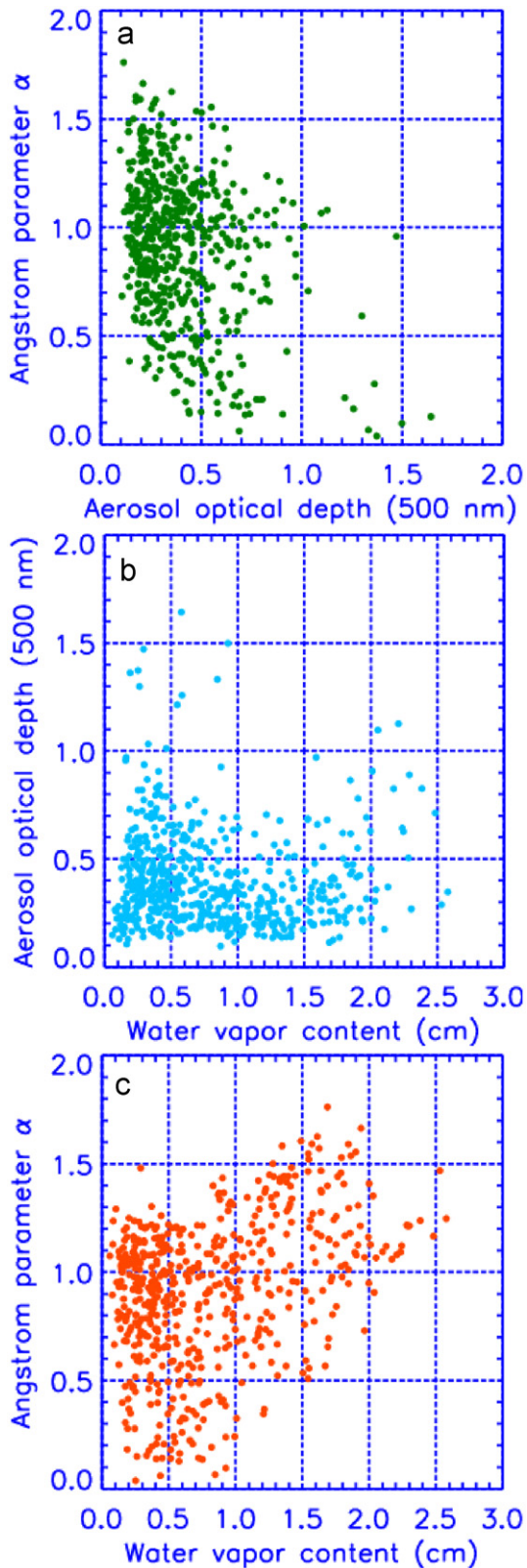
**Fig. 7.** Diurnal cycle of seasonal mean aerosol optical depth at the 500 nm wavelength for the period of August 2006–October 2008.



**Fig. 8.** Diurnal cycle of seasonal mean Ångström exponent (α) for period of August 2006–October 2008.



**Fig. 6.** Scatterplots of (a) Ångström exponent versus aerosol optical depth, (b) aerosol optical depth versus water vapor path, and (c) Ångström parameter versus water vapor path.
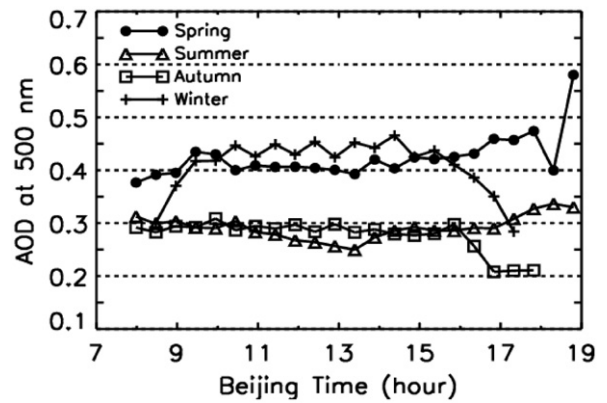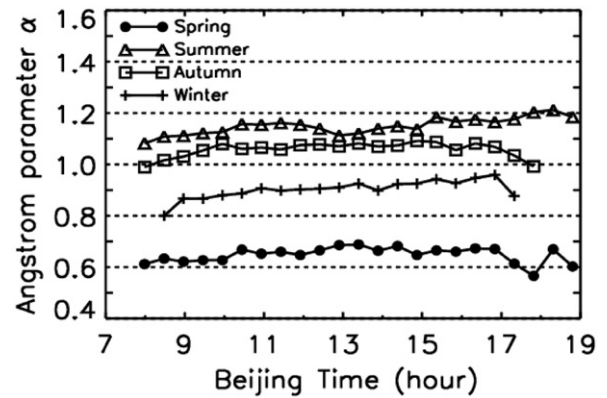
1.15( ± 0.312), 1.06( ± 0.197), and 0.909( ± 0.246) for spring, summer, autumn, and winter, respectively. It suggests that the fine particles contribute more relative to large aerosols in summer and autumn seasons, while the coarse particles are the dominant parts in spring. The mean Ångström exponent value of springtime is about 77.2% and 63.3% less than in summer and autumn, respectively. The difference is related to summer–autumn rainfall and spring dust weather events.

The total column-integrated water vapor amounts also show significant seasonal variability (Fig. 5). The distribution is wider in Summer and autumn seasons, while the winter's distribution is narrowest. The winter season's frequency distribution has a modal value of 0.25–0.5 cm. The modal value in spring season is 0.75 cm. The 2-year averaged WVP is 0.77 cm, and seasonal mean are 0.609( ± 0.293), 1.40( ± 0.391), 0.727( ± 0.372), and 0.245( ± 0.095) for spring, summer, autumn, and winter, respectively.

The scatterplot of daily averaged aerosol optical depth versus Ångström exponent is shown Fig. 6a, which may allow one to define physically interpretable cluster regions for different types of aerosols [32]. Although no obvious cluster discrimination is evident in Fig. 6a, one
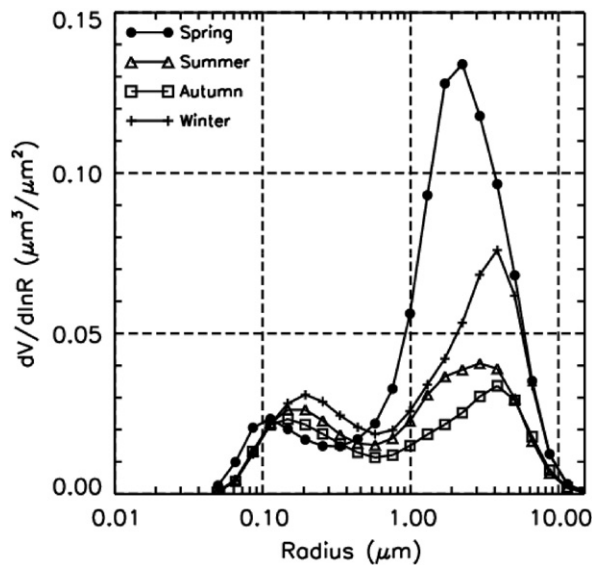
Fig. 9. Seasonal aerosol volume size distributions in the total atmospheric column.



Fig. 10. Mean monthly aerosol volume size distributions in the total atmospheric column (N is the number of averaged retrievals).

feature is worth nothing: a wide range of $\alpha$ at moderate to low aerosol optical depths ($<0.8$). The daily averaged WVP and aerosol optical depth at 500 nm (Fig. 6b) shows no significant correlation. This may be because aerosol and water vapor are transported at different altitudes about SACOL site and/or from several source regions with differing seasonal combinations of $\tau_a$ and WVP.

The scatterplot of $\alpha$ versus WVP (Fig. 6c) shows a generally positive correlation. Since the aerosol particle should become larger when the water vapor increases, Fig. 6c again indicates that the water vapor and aerosols may be located at different heights or aerosols are from different source regions. For example, the dust aerosols that have larger sizes than sulfate and soot aerosols are usually accompanied by dry air.

## 3.2. Diurnal dependences of aerosol optical properties and water vapor path

The diurnal variability of atmospheric optical properties and precipitable water may be of greatly importance for various applications. Also, the hourly statistics themselves are of interest for atmospheric correction and validation efforts. Using our data sets we computed the diurnal dependences of $\tau_a$ (500 nm), $\alpha$, and WVP according to the following procedure. All individual observations were averaged over a half-hour (07:00–07:30, 07:30–08:00 local time, etc.) for given season. So we can acquire the systematic diurnal cycle of all seasons.

The diurnal cycle of aerosol optical depth at 500 nm is shown in Fig. 7 for each season. They are relatively stable in the daytime. In wintertime, the mean values of AOD are small in the morning and evening, which are lower than 0.3, and it is large during the daytime (varying within 0.4–0.5 range). The diurnal dependences in the summer
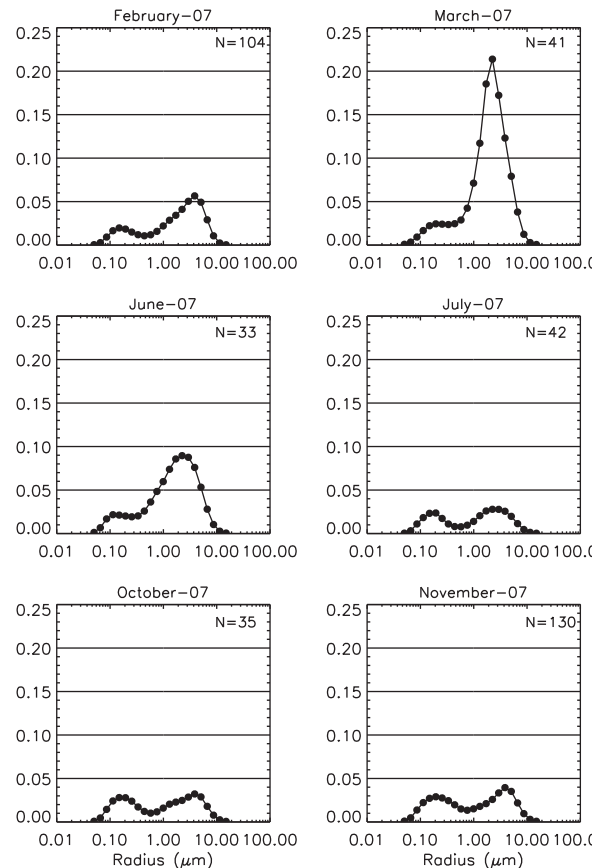
and autumn seasons are rather small before late afternoon, which vary within 0.25–0.3 range. However, in the afternoon after about 16:00 p.m., the mean values vary relatively large, which have an optical depth of 0.2 and 0.35, respectively, in the autumn and summer. These results are similar to Huang et al. [22]. It is worth noting that there is a high value ($\sim0.60$) at 19:00 p.m. in spring. This may be due to the measurements that have a higher chance of cloud contamination during low sun elevation angles [28].

Fig. 8 is similar to Fig. 7 but for Ångström exponent. The Ångström exponent is gradually digression for summer, autumn, winter, to spring season. In spring, diurnal variations of Ångström exponent present stable low value during daytime. The variability in summer is larger than other seasons. In autumn the values of $\alpha$ vary between 1.0 and 1.1. In winter, the values vary between 0.8 and 1.0 (Fig. 8).

The diurnal cycles of water vapor path are also evident. The largest diurnal variation of WVP appears in autumn, which varies between 0.60 to 1.3 cm range, with large values of 0.9 cm in the morning and 1.3 cm in the afternoon. It is related to the rainy in that season. Although it is also rainy season in summer, the diurnal cycle is relatively small, varying within 1.3–1.6 cm. It is
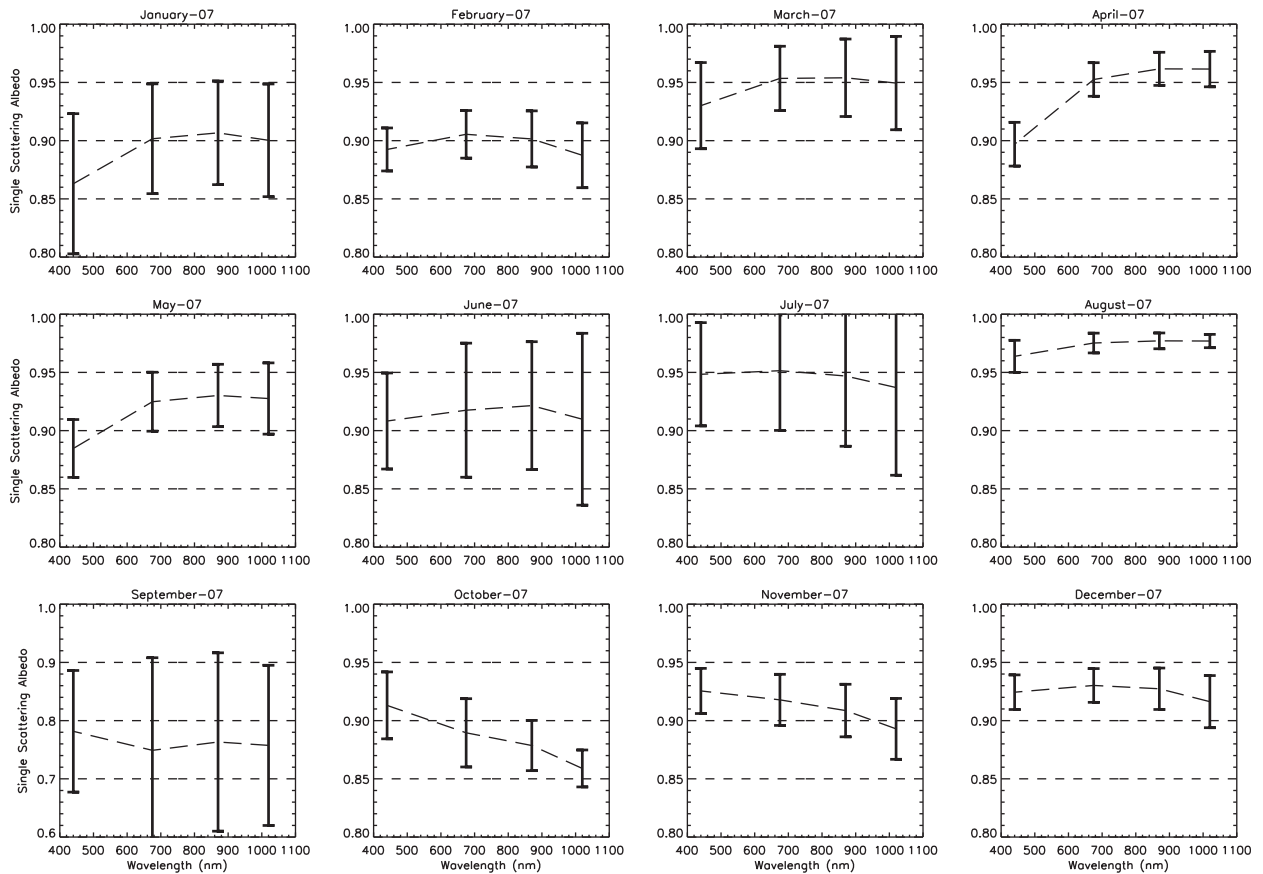
**Fig. 11.** Mean monthly spectral values of the retrieved single scattering albedos (corresponding to AOD at 440 nm > 0.4).

due to the uniform rainfall in the whole season. The variations of spring are very small before the late afternoon, which vary within 0.6–0.7 cm, but have a large value of 1.0 cm in the late afternoon. The diurnal variation is extremely small in the winter, with a WVP of about 0.2–0.3 cm.

### 3.3. Aerosol microphysical properties and optical spectral dependences

Aerosol microphysical and optical properties including aerosol volume size distributions, single scattering albedos, asymmetry parameter, real and imaginary parts of complex refractive indices were retrieved from spectral sun and sky radiance observations. This is achieved by iterative inversion algorithms [26]. The initial guesses of $dV/d \ln R = 0.0001$, $n(\lambda_i) = 1.50$, $k(\lambda_i) = 0.005$ are used, where $dV/d \ln R$ denotes aerosol volume size distribution, and $n(\lambda_i)$ and $k(\lambda_i)$ denotes real and imaginary parts of the refractive index at a wavelength $\lambda_i$ [32]. The retrieved quantities corresponding to the effective microphysical/optical properties of the total atmospheric column. In the retrieval algorithm the aerosol particles are assumed to be a shape mixture of randomly oriented polydisperse spheroids.

Dubovik and King [26] showed that the size distribution, in the case of nonspherical dust aerosols, can be retrieved

reasonably well when the angular range of sky radiances is limited to scattering angles smaller than 30–40°. However, in order to retrieve SSA the sky radiances acquired in the whole almucantar are needed along with the direct sun measurements. Thus for nonspherical dust aerosols, we should use the early morning or late afternoon sky radiance measurements when the scattering angle range is large to retrieve a single scattering albedo. The AERONET's retrieval algorithm does not rely on Mie scattering but is instead based on the model of polydispersed, randomly oriented spheroids. The results using AERONET measurements taken at several dust-dominated locations has shown significant improvements in the retrieved size distribution, single scattering albedo, refractive index, and phase function of dust like aerosol particles [33]. We used the sky radiances acquired around midday when scattering angle range is small to extract aerosol size distributions [26].

Figs. 9 and 10 show seasonal and monthly averaged size distributions ($dV/d \ln R$). The variations in these distributions are largely associated with changes in the amplitude and spectral dependence of the aerosol optical depth. The fine mode shows relative stability, while the coarse fraction changes significantly. The variation of the magnitude and shape of the coarse aerosol fraction in springtime is mainly attributed to incoming dust (Fig. 9). The fine aerosol fraction changed as well, but there were

**Table 1**
Monthly mean parameters of aerosol volume size distributions.

| | Fine mode | | | | Coarse mode | | | |
|---|---|---|---|---|---|---|---|---|
| | $C_v^a$ | $R_v^b (\mu m)$ | $R_{eff}^c (\mu m)$ | $\sigma^d$ | $C_v^a$ | $R_v^b (\mu m)$ | $R_{eff}^c (\mu m)$ | $\sigma^d$ |
| August 2006 | 0.071 | 0.216 | 0.189 | 0.506 | 0.064 | 2.57 | 2.08 | 0.657 |
| September 2006 | 0.036 | 0.182 | 0.160 | 0.510 | 0.063 | 2.29 | 1.80 | 0.692 |
| October 2006 | 0.036 | 0.184 | 0.162 | 0.514 | 0.054 | 2.49 | 1.94 | 0.700 |
| November 2006 | 0.035 | 0.181 | 0.158 | 0.521 | 0.068 | 2.71 | 2.10 | 0.693 |
| Dec 2006 | 0.056 | 0.253 | 0.215 | 0.563 | 0.071 | 2.78 | 2.31 | 0.604 |
| January 2007 | 0.039 | 0.193 | 0.172 | 0.477 | 0.155 | 2.77 | 2.19 | 0.657 |
| February 2007 | 0.028 | 0.178 | 0.158 | 0.492 | 0.096 | 2.59 | 1.99 | 0.708 |
| March 2007 | 0.041 | 0.198 | 0.172 | 0.515 | 0.295 | 2.14 | 1.75 | 0.625 |
| April 2007 | 0.027 | 0.174 | 0.146 | 0.592 | 0.340 | 2.30 | 1.86 | 0.635 |
| May 2007 | 0.029 | 0.157 | 0.137 | 0.531 | 0.186 | 2.37 | 1.85 | 0.690 |
| June 2007 | 0.039 | 0.170 | 0.150 | 0.507 | 0.180 | 2.12 | 1.64 | 0.723 |
| July 2007 | 0.032 | 0.182 | 0.165 | 0.457 | 0.053 | 2.57 | 2.03 | 0.674 |
| Aug 2007 | 0.071 | 0.218 | 0.194 | 0.481 | 0.083 | 2.30 | 1.89 | 0.631 |
| September 2007 | 0.031 | 0.163 | 0.146 | 0.465 | 0.052 | 2.63 | 2.00 | 0.731 |
| October 2007 | 0.043 | 0.182 | 0.160 | 0.500 | 0.059 | 2.58 | 2.00 | 0.715 |
| November 2007 | 0.051 | 0.205 | 0.177 | 0.538 | 0.063 | 2.96 | 2.34 | 0.670 |
| December 2007 | 0.066 | 0.198 | 0.168 | 0.570 | 0.146 | 2.83 | 2.30 | 0.626 |
| January 2008 | 0.068 | 0.193 | 0.167 | 0.521 | 0.137 | 2.97 | 2.38 | 0.643 |
| February 2008 | 0.057 | 0.239 | 0.210 | 0.486 | 0.088 | 2.69 | 2.12 | 0.675 |
| March 2008 | 0.037 | 0.145 | 0.127 | 0.533 | 0.192 | 2.31 | 1.83 | 0.678 |
| April 2008 | 0.043 | 0.150 | 0.132 | 0.532 | 0.175 | 2.20 | 1.75 | 0.672 |
| May 2008 | 0.039 | 0.152 | 0.133 | 0.534 | 0.197 | 2.26 | 1.80 | 0.661 |
| June 2008 | 0.027 | 0.149 | 0.134 | 0.481 | 0.077 | 2.27 | 1.77 | 0.705 |
| July 2008 | 0.046 | 0.191 | 0.169 | 0.482 | 0.052 | 2.82 | 2.27 | 0.658 |
| August 2008 | 0.037 | 0.163 | 0.145 | 0.486 | 0.062 | 2.55 | 2.06 | 0.652 |
| September 2008 | 0.022 | 0.170 | 0.149 | 0.516 | 0.037 | 2.80 | 2.22 | 0.688 |
| October 2008 | 0.025 | 0.173 | 0.155 | 0.477 | 0.048 | 2.39 | 1.88 | 0.692 |
| Mean | 0.042 | 0.184 | 0.161 | 0.511 | 0.115 | 2.53 | 2.01 | 0.672 |
| Std. dev. | 0.014 | 0.026 | 0.022 | 0.032 | 0.078 | 0.252 | 0.208 | 0.032 |
| Var. coef. | 0.333 | 0.141 | 0.137 | 0.063 | 0.678 | 0.100 | 0.103 | 0.048 |

$^a C$ is the volume concentration ($\mu m^3 \mu m^{-2}$); $^b R$ is the volume geometric mean radius; $^c R_{eff}$ is the effective radius; $^d \sigma$ is the geometric std. dev.

no-significant changes in the magnitude and shape of size distributions. The fine mode geometric mean radius in March 2008 was smaller (see Table 1). This may be due to the non-sphericity of aerosols, which may appear when desert dust aerosol dominates [26].

Table 1 shows parameters of the bimodal lognormal volume size distributions [34,35] shown in Figs. 9 and 10. For each mode the lognormal distribution is defined as

$$\frac{dV}{d\ln R} = \frac{C_v}{\sigma\sqrt{2\pi}} \exp\left[ -\frac{1}{2}\left(\frac{\ln(R/R_v)}{\sigma}\right)^2 \right],$$

where $dV/d\ln R$ is the volume distribution, the volume concentration $C_v$ is the columnar volume of particles per unit cross section of atmospheric column, $R$ is the particle radius, $R_v$ is the volume geometric mean radius, and $\sigma$ is the geometric standard deviation. Effective radius is defined as a ratio of the third over the second moment of the number size distribution. It should be noted that we assigned particles with radii $0.05 < r < 0.3$–$0.6 \mu m$ and with radii $0.3$–$0.6 < r < 15 \mu m$ to the fine and coarse modes, respectively. Volume concentrations for each fraction are also shown in Table 1.

Variations in aerosol volume size distributions were largely due to changes in the concentration of both coarse

aerosol fraction (with variation coefficient[1] of 68%) and the fine aerosol fraction (with variation coefficient of 33%). The annual averaged particle fine and coarse mode geometric mean radii were 0.18 (std. dev.=0.03) and 2.53 μm (std. dev.=0.25), respectively. Variation coefficients are 14% for the fine mode $R_v$ and 6.3% for the fine mode $\sigma$, and 10% and 4.8% for the coarse mode parameters (Table 1).

The aerosol single scattering albedo (SSA), defined as the ratio between the particle scattering coefficient and the total extinction coefficient is usually used to characterize the aerosol absorption properties and is a key variable in assessing the radiative forcing of aerosols. The SSA is mainly dependent on the chemical composition, size distribution and matter concentration of aerosol particles. The monthly averages of SSA (corresponding to AOD at 440 nm > 0.4) are shown in Fig. 11. The vertical bars indicate plus or minus one standard deviation.

Two major features of the SSA spectral dependence can be observed. When dust is not the major contributor to

---

[1] Variation coefficient here is defined as standard deviation divided by the mean.

the atmospheric aerosols, the SSA decreases with wave-length. The SSA in October and November systematically show this type of spectral dependence. In the presence of dust from March to May, the SSA increases with the wavelength at 440–670 nm range but the spectral dependence of the SSA is almost neutral for the wave-length longer than 1020 nm. Such spectral dependence is also evident in January. An increase of single scattering albedo with wavelength can be caused by the domination of coarse dust particle mode (e.g., Ackerman and Toon [43]) and by higher absorption in the blue spectral band [36], Levin et al. [37] reported low absorption of the dust aerosol in the center of the visible spectral range. For the dust aerosols at SACOL, the results show relatively weak absorption within the 670–1100 nm spectral range. Otherwise, the monthly mean values of SSA vary within 0.85–1.00 range, except for September 2007, which varies within 0.75–0.80 range.

The retrieved real and imaginary parts of complex refractive indices for aerosol particles reflect the ability of scattering and absorption to incoming radiation, respec-tively. There are different complex refractive indices for aerosol particles with different chemical components. Figs. 12 and 13 show the monthly mean spectral values of the retrieved real part and imaginary part of refractive

indices, respectively. The monthly average values of real part vary within 1.4–1.6 range for the whole period with a weak wavelength dependence. Comparing with the variations of real part, the imaginary part of aerosol particles has much larger dependence on wavelength. The averaged values of imaginary part are relatively large during September–November 2007, which vary in the 0.01–0.04 range. It suggests that there are amount of absorbing fine particles in the atmosphere for these seasons. In the spring, the imaginary part displays relatively low value (~0.005), which indicates dust coarse particles has rather weak absorbing properties in SACOL region.

The asymmetry parameter represents the first moment of the particle scattering phase function. For cloudless atmosphere, the value of asymmetry factor ranges from 0.1 under very clean conditions to 0.75 in the polluted situations ([38]). Fig. 14 shows the monthly mean spectral values of retrieved asymmetry parameter. The monthly averaged values of asymmetry parameter vary within 0.65–0.75 range for the whole period. It is a notable characteristic that asymmetry parameter decreases with wavelength at 440–1020 nm range for all months 2007. However, the decreasing trend is smaller in the wavelength range 670–1020 nm during the spring. This is
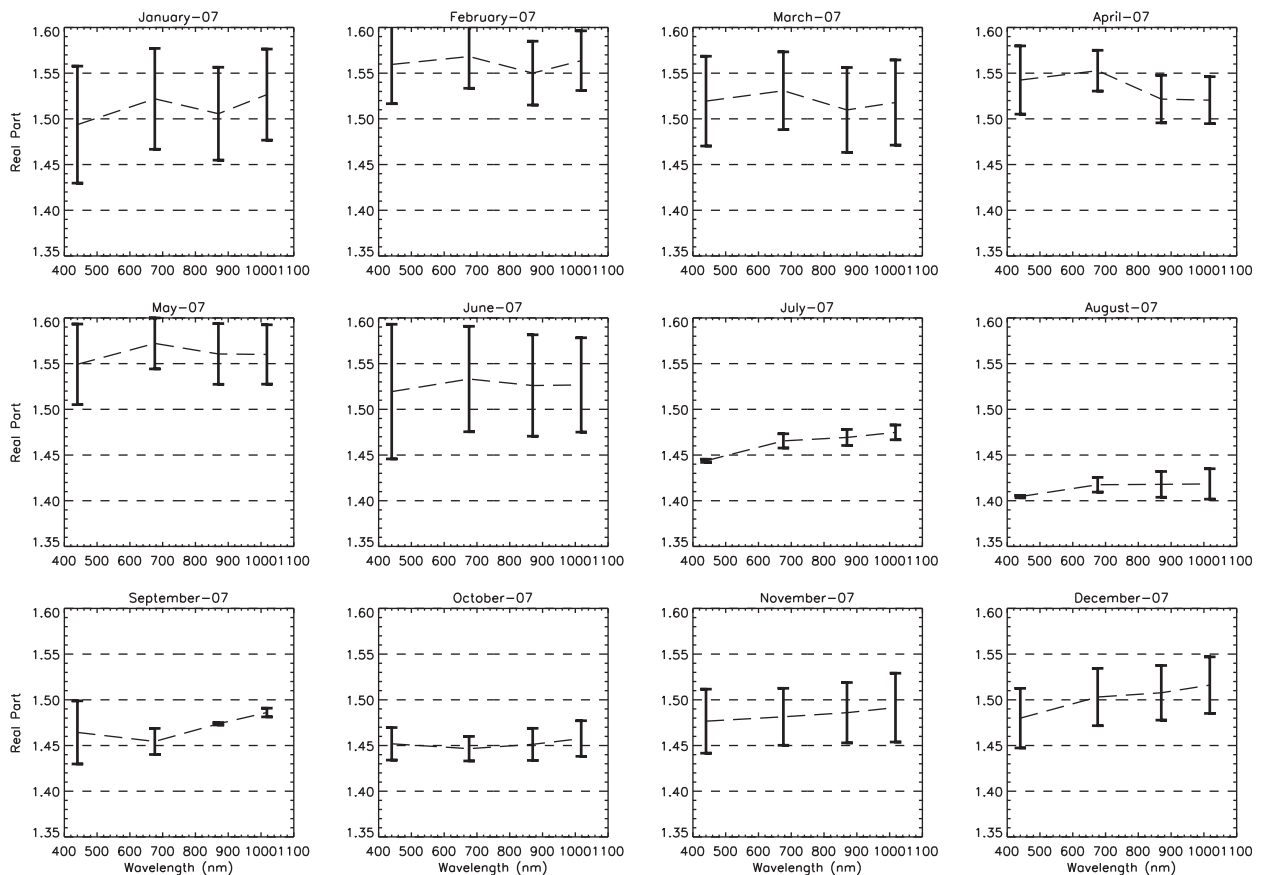


Fig. 12. Mean monthly spectral values of the retrieved real part of refractive indices.
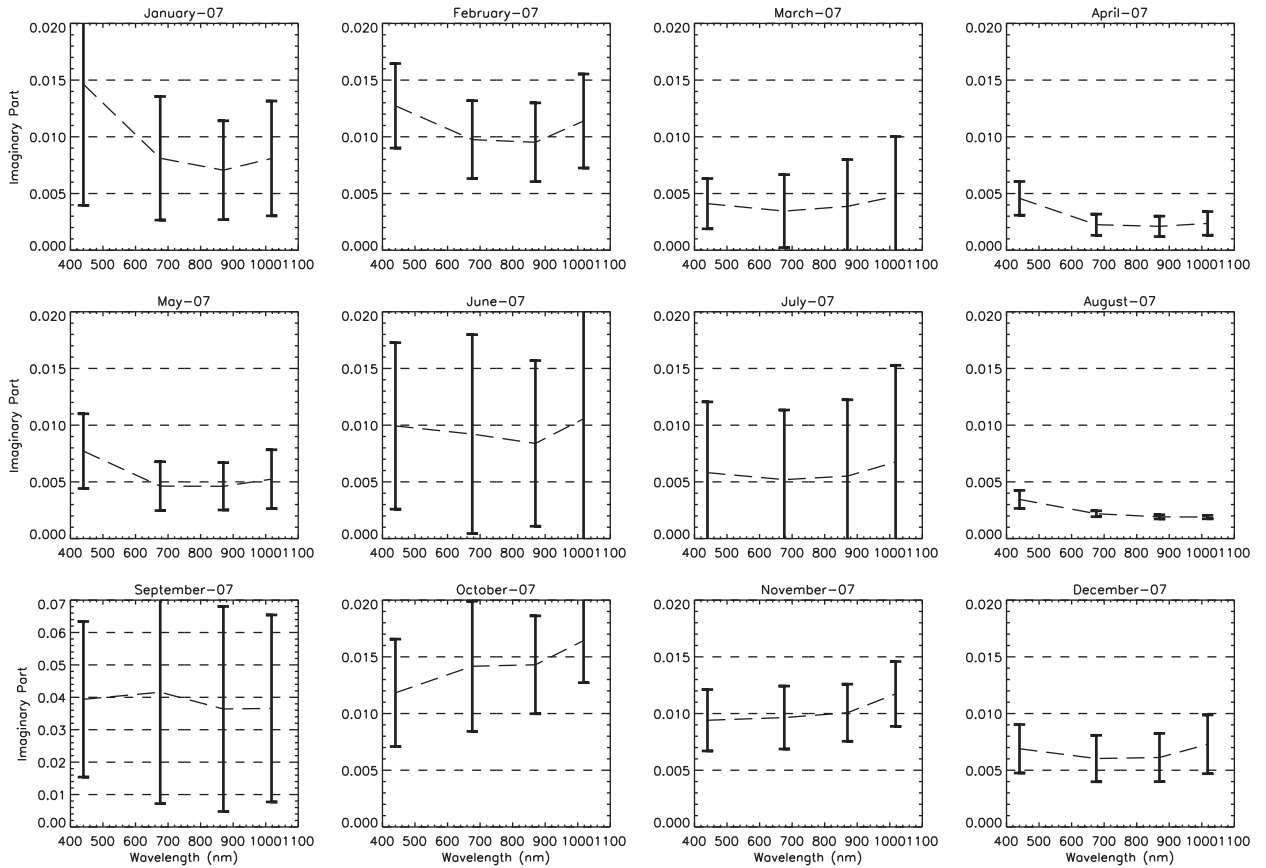
Fig. 13. Mean monthly spectral values of the retrieved imaginary part of refractive indices.

due to the contribution of coarse particles in the frequent dust weather. The asymmetry factors of coarse particles were larger than those of fine particles for given AOD.

Fig. 15 shows seasonally averaged spectral values of the retrieved single scattering albedo, asymmetry parameter, the real and imaginary parts of refractive indices, and asymmetry parameters of fine particles and coarse particles, respectively. The seasonal mean values of SSA vary with 0.87–0.96 range. In spring, the SSA preserves high values and increases slightly with wavelength due to the contribution of coarse particles. But the SSA decreases with spectra in the other seasons, except for the value increases from 440 to 675 nm wavelength in winter. The seasonal average values of asymmetry parameters vary within 0.65–0.75 range. It is a notable characteristic that the asymmetry factors decrease with wavelength from 440 to 1020 nm range. In the presence of dust the spectral dependence of asymmetry factor is almost constant at 670–1020 nm range. The seasonal averages of real part and imaginary part vary within 1.45–1.52, and 0.003–0.013 range, respectively. In spring, the real part increases from 440 to 675 nm wavelength, and decreases with wavelength at 675–1020 nm. In summer, the real part keeps almost constant at 670–1020 nm

range. In autumn and winter, the real part increases from 440 to 675 nm and decreases from 675 to 870 nm, and increases from 870 to 1020 nm again. The seasonal variability of imaginary part is apparent, which is gradually decreased from autumn, winter, summer, to spring season. For fine particles, the asymmetry factors decrease linearly with 440–1020 nm range. And the same is for the coarse aerosol particles.

The aerosol phase function describes the angular distribution of scattering energy. The impact of non-sphericity on phase function has been shown to depend on the scattering angle ([39]). Fig. 16(a) shows the seasonal averages of phase function for different scattering angle at 676 nm wavelength. The minimum value of phase function appears at the scattering angle of around 130° (see Fig. 16(b)) and the maximum value occurs at the scattering angle of 0° for all the seasons.

Table 2 shows the seasonally averaged phase functions at scattering angles of 0°, 90°, 120°, and 180° for fine ($r < 0.6\,\mu m$) and coarse ($r > 0.6\,\mu m$) particles at 676 nm. It indicates that the phase function has a high sensitivity to scattering angles for both fine and coarse particles at SACOL for all seasons. From Table 2, we also know that the values of phase functions at scattering angle 120° are the least in all seasons. The scattering phase functions of coarse
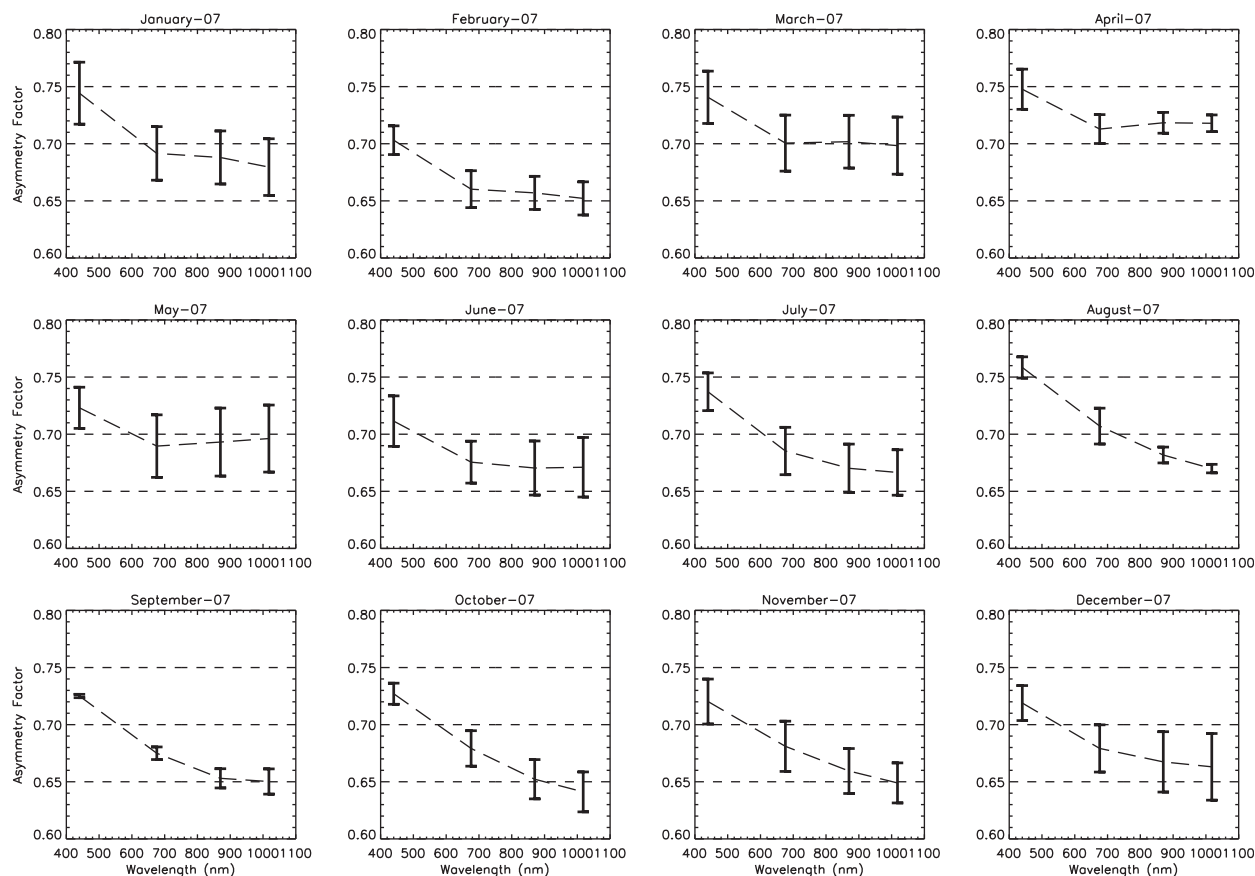
**Fig. 14.** Mean monthly spectral values of the retrieved asymmetry parameter.

particles at forward and backward directions are larger than those of fine particles due to larger sizes, with values of 382.08 at 0° and 0.33 at 180° for coarse particles, and lower values of 9.10 at 0° and 0.25 at 180° for fine particles.

## 4. Conclusions and discussion

The main conclusions of this study can be summarized as follows.

The seasonal variability of the aerosol optical and microphysical properties is significant over Loess Plateau of Northwest China. These variations show that the dust aerosol concentrations in spring and the anthropogenic aerosols in the other seasons are the major contributors to AOD, Ångström exponent, volume size distribution and single scattering albedo variability. The 2-year (August 2006–October 2008) average values of AOD and Ångström exponent are 0.35 and 0.93, respectively. The probability distribution functions of AOD, Ångström exponent, and WVP have one modal value, which are 0.3, 1.1, and 0.5 cm, respectively.

Pinker et al. [40] analyzed aerosol radiative properties in the semiarid West United States (Tombstone Arizona site) by using the CIMEL sun photometer data for 1-year period. Their results suggest that monthly mean AODs at 500 nm vary within 0.03–0.12 range. Holben et al. [41] indicated that the mean annual AOD at 500 nm is 0.08 at Sevilleta, New Mexico (which is located in the arid intermountain basin of the American Southwest) for the period of 1994–1999. Although the semiarid regions between China and the USA have similar climatic conditions, but our study suggests that multi-year mean AOD at 500 nm over the semiarid area of northwest China is 0.35, which is much higher than that over the USA. This is because aerosols in the semiarid region in Northwestern China not only contain local anthropogenic aerosols (agricultural dust, industrial black carbon, and other anthropogenic aerosols), but also include dust transported from desert regions. Huang et al. [42] presents that the mean spring AOD derived from MODIS over the CSR (semiarid region in Northwestern China) is 0.30, which is 65.9% higher than that over the USR (semiarid region in the USA). The ground-based measurements confirm the study by Huang et al. [42] based on satellite observations.

There is a notable feature in the relationship between daily averaged AOD and Ångström exponent: a wide range of $\alpha$ at moderate to low aerosol optical depths ( < 0.8). The relationship between daily averaged WVP and AOD shows
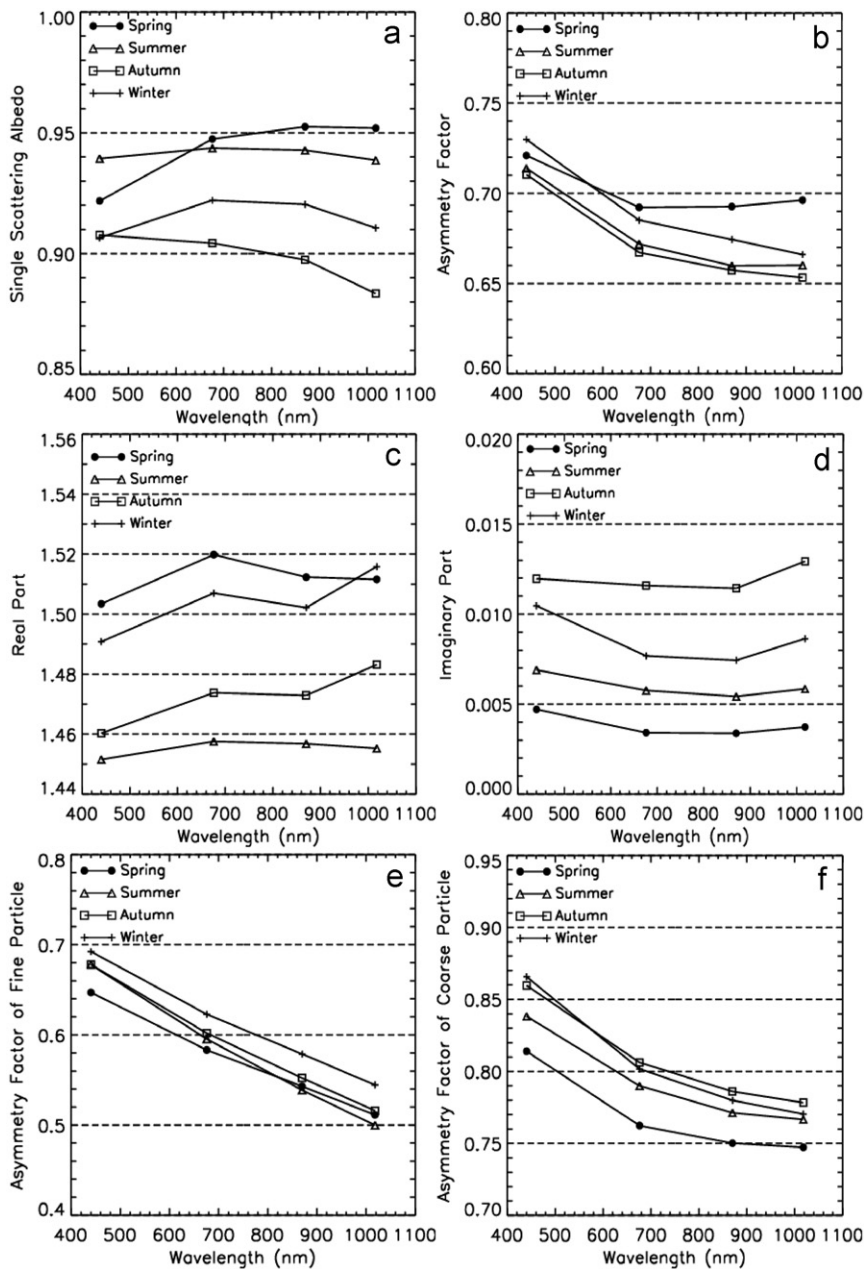
**Fig. 15.** Seasonal spectral values of the retrieved (a) single scattering albedo, (b) asymmetry parameter, (c) the real and (d) imaginary parts of refractive indices, (e) asymmetry parameters of fine particles, and (f) coarse particles.

no significant correlation. The scatterplot of daily averaged Ångström exponent and WVP indicates a significant positive correlation, due to large dust aerosol particles associated with dry air.

Optical inversions of sky radiance and optical depth datum indicate that the variations in aerosol volume size distributions at SACOL are largely due to changed in the concentration of the coarse aerosol fraction (variation coefficient of 68%). There is apparent

bimodal lognormal volume size distribution for the whole period. And the annual average particle fine and coarse mode geometric mean radii are 0.18 (std. dev.=0.03) and 2.53 μm (std. dev.=0.25), respectively.

The spectral dependences of single scattering albedos are different between the dusty and non-dusty conditions. In the presence of dust, the SSAs increase with wavelength. When dust is not a major component, the corresponding values decrease with wavelength.
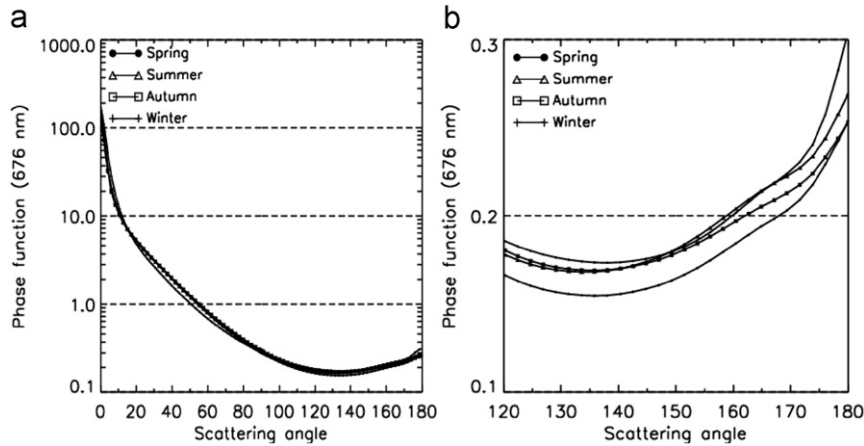
**Fig. 16.** Seasonal averages of phase function from scattering angle (a) 0–180° and (b) 120–180° at 676 nm wavelength.

**Table 2**
Phase functions at 676 nm wavelength for fine ($r < 0.6$ µm) and coarse ($r > 0.6$ µm) particles.

| | Fine particles | | | | Coarse particles | | | |
|---|---|---|---|---|---|---|---|---|
| | 0° | 90° | 120° | 180° | 0° | 90° | 120° | 180° |
| Spring | 8.652 | 0.374 | 0.239 | 0.275 | 280.807 | 0.222 | 0.146 | 0.343 |
| Summer | 8.643 | 0.358 | 0.218 | 0.254 | 354.308 | 0.181 | 0.110 | 0.333 |
| Autumn | 9.025 | 0.356 | 0.212 | 0.243 | 433.521 | 0.170 | 0.104 | 0.303 |
| Winter | 9.958 | 0.333 | 0.192 | 0.230 | 458.284 | 0.176 | 0.108 | 0.340 |
| Year | 9.107 | 0.355 | 0.215 | 0.250 | 382.083 | 0.188 | 0.118 | 0.331 |
| Std. | 2.343 | 0.060 | 0.052 | 0.054 | 134.878 | 0.037 | 0.031 | 0.137 |

## Acknowledgements

## References

[1] Jacovides CP, Kassomenos P, Kaltsunideset NA. Estimate of effective aerosol optical depths from spectral solar radiation measurements. Theor Appl Climatol 1996;53:211–20.

[2] Tegen I. Modeling the mineral dust aerosol cycle in the climate system. Quat Sci Rev 2003;22(19):1821–34, doi:10.1016/S0277-3791(03)00163-X.

[3] Slingo A, Ackerman TP, Allan RP, Kassianov EI, McFarlane SA, Robinson GJ, et al. Observations of the impact of a major Saharan dust storm on the atmospheric radiation balance. Geophys Res Lett 2006;33:L24817, doi:10.1029/2006GL027869.

[4] Li Z, Chen H, Cribb M, Dickerson R, Holben B, Li C, et al. Preface to special section: overview of the East Asian study of tropospheric aerosols: an international regional experiment (EAST-AIRE). J Geophys Res 2007;112:D22S00, doi:10.1029/2007JD008853.

[5] Huang J, Minnis P, Lin B, Wang T, Yi Y, Hu Y, et al. Possible influences of Asian dust aerosols on cloud properties and radiative forcing observed from MODIS and CERES. Geophys Res Lett 2006;33:L06824, doi:10.1029/2005GL024724.

[6] Huang J, Wang Y, Wang Y, Yi Y. Dusty cloud radiative forcing derived from satellite data from middle latitude regions of East Asia. Prog Nat Sci 2006;16(10):1084–9.

[7] Andreae MO. Raising dust in the greenhouse. Nature 1996;380: 389–90.

[8] Ramanathan V, Crutzen PJ, Kiehl JT, Rosenfeld D. Aerosols, climate and the hydrologic cycle. Science 2001;294:2119–24.

[9] Li Z, Xia X, Cribb M, Mi W, Holben B, Wang P, et al. Aerosol optical properties and their radiative effects in northern China. J Geophys Res 2007;112(D22S01)10.1029/2006JD007382.

[10] Twomey SA, Piepgrass M, Wolfe TL, et al. An assessment of the impact of pollution on global cloud albedo. Tellus B 1984;36:356–66.

[11] Intergovernmental Panel on Climate Change. Climate change 2007: The scientific basis – contribution of working group I to the fourth assessment report of the intergovernmental panel on climate change. In: Solomon S. et al., editor. New York: Cambridge University Press; 2007. 1056 pp.

[12] Nakajima T, Sekiguchi M, Takemura T, Uno I, Higurashi A, Kim D, et al. Significance of direct and indirect radiative forcings of aerosols in the East China Sea region. J Geophys Res 2003;108(D23):8658, doi:10.1029/2002JD003261.

[13] Zhang XY, Gong SL, Zhao TL, Arimoto R, Wang YQ, Zhou ZJ. Sources of Asian dust and role of climate change versus desertification in Asian dust emission. Geophys Res Lett 2003;30:2272, doi:10.1029/2003GL018206.

[14] Huang J, Minnis P, Yi Y, Tang Q, Wang X, Hu Y, et al. Summer dust aerosols detected from CALIPSO over the Tibetan Plateau. Geophys Res Lett 2007;34:L18805, doi:10.1029/2007GL029938.

[15] Uematsu M, Duce RA, Prospero JM, Chen L, Merrill JT, McDonald RL. Transport of mineral aerosol from Asia over the North Pacific Ocean. J Geophys Res 1983;88:5343–52.

[16] Iwasaka Y, Minoura H, Nagaya K. The transport and spatial scale of Asian dust-storm clouds: a case study of the dust-storm event of April 1979. Tellus 1988;35B:189–96.

[17] Husar RB, Prospero JM, Stowe LL. Characterization of tropospheric aerosols over the oceans with the NOAA advanced very high resolution radiometer optical thickness operational product. J Geophys Res 1997;102(D14):16,889–909, doi:10.1029/96JD04009.

[18] Kim DH, Sohn BJ, Nakajima T, Takamura T, Takemura T, Choi BC, et al. Aerosol optical properties over East Asia determined from ground-based sky radiation measurements. J Geophys Res 2004;109:D02209, doi:10.1029/2003JD003387.

[19] Eck TF, Holben BN, Dubovik O, Smirnov A, Goloub P, Chen HB, et al. Columnar aerosol optical properties at AERONET sites in central eastern Asia and aerosol transport to the tropical mid-Pacific. J Geophys Res 2005;110:D06202, doi:10.1029/2004JD005274.

[20] Xin J, Wang S, Wang Y, Yuan J, Zhang W, Sun Y. Optical properties and size distribution of dust aerosols over the Tengger Desert in Northern China. Atmos Environ 2005;39:5971–8.

[21] Xia XA, Chen HB, Wang PC, Zong XM, Gouloub P. Aerosol properties and their spatial and temporal variations over north China in spring 2001. Tellus B 2005;57:28–39.

[22] Huang J, Zhang W, Zuo J, Bi J, Shi J, Wang X, et al. An overview of the Semi-Arid Climate and Environment Research Observatory over the Loess Plateau. Advances in Atmospheric Sciences 2008;25(6): 1–16.

[23] Holben BN, et al. AERONET—a federated instrument network and data archive for aerosol characterization. Remote Sensing Environ 1998;66:1–16.

[24] Eck TF, Holben BN, Reid JS, Dubovik O, Smirnov A, O'Neill NT, et al. Wavelength dependence of the optical depth of biomass burning, urban and desert dust aerosols. J Geophys Res 1999;104:31333–50.

[25] Schmid B, Michalsky JJ, Slater DW, Barnard JC, Halthore RN, Liljegren JC, et al. Comparison of columnar water vapor measurements from solar transmittance methods. Applied Optics 2001;40(12):1886–96.

[26] Dubovik O, King MD. A flexible inversion algorithm for the retrieval of aerosol optical properties from Sun and sky radiance measurements. J Geophys Res 2000;105:20673–96.

[27] Dubovik O, Smirnov A, Holben BN, King MD, Kaufman YJ, Eck TF, et al. Accuracy assessments of aerosol optical properties retrieved from AERONET sun and sky radiance measurements. J Geophys Res 2000;105:9791–806.

[28] Smirnov A, Holben BN, Eck TF, Dubovik O, Slutsker I. Cloud screening and quality control algorithms for the AERONET data base. Remote Sensing Environ 2000;73(3):337–49.

[29] King MD, Byrne DM. A method for inferring total ozone content from spectral variation of total optical depth obtained with a solar radiometer. J Atmos Sci 1976;33:2242–51.

[30] Kaufman YJ. Aerosol optical thickness and atmospheric path radiance. J Geophys Res 1993;98:2677–92.

[31] O'Neill NT, Eck TF, Holben BN, Smirnov A, Dubovik O, Royer A. Bimodal size distribution influences on the variation of Angstrom derivatives in spectral and optical depth space. J Geophys Res 2001;106:9787–806, doi:10.1029/2000JD900245.

[32] Smirnov A, Holben BN, Dubovik O, O'Neil NT, Eck TF, Westphal DL, et al. Atmospheric aerosol optical properties in the Persian Gulf. J Atmos Sci 2002;59:620–34.

[33] Dubovik O, Holben BN, Lapyonok T, Sinyuk A, Mishchenko MI, Yang P, et al. Non-spherical aerosol retrieval method employing light scattering by spheroids. Geophys Res Lett 2002;29(10): 54, doi:10.1029/2001GL014506.

[34] Whitby KT. The physical characteristics of sulfur aerosols. Atmos Environ 1978;12:135–59.

[35] Remer LA, Kaufman YJ, Holben BN. Interannual variation of ambient aerosol characteristics on the east coast of the United States. J Geophys Res 1999;104:2223–31.

[36] Kaufman YJ, Tanre D, Dubovik O, Karnieli A, Remer LA. Satellite and ground based radiometers reveal much lower dust absorption of sunlight than used in climate models, Geophys Res Lett, 2001;28:1479–83.

[37] Levin Z, Joseph JH, Mekler Y. Properties of Sharav (Khamsin) dust—comparison of optical and direct sampling data. J Atmos Sci 1980;37:882–91.

[38] Zege EP, Ivanov AP, Katsev IL. In: Image transfer through a scattering medium. New York: Springer-Verlag; 1991.

[39] Nakajima T, Tanaka M, Yamano M, Shiobara M, Arao K, Nakanishi Y. Aerosol optical characteristics in the yellow sand events observed in May, 1982 at Nagasaki, part 2, models. J Meteorol Soc Japan 1989;67:279–91.

[40] Pinker RT, Pandithurai G, Holben BN, Keefer TO, Goodrich D. Aerosol radiative properties in the semiarid Western United States. Atmos Res 2004;71(2004):243–52.

[41] Holben BN, Tanre D, Smirnov A, Eck TF, Slutsker I, Abuhassan N, et al. An emerging ground-based aerosol climatology: aerosol optical depth from AERONET. J Geophys Res 2001;106:12,067–97.

[42] Huang J, Patrick Minnis, Yan H, Yi Y, Chen B, Zhang L, et al. Dust aerosol effect on semi-arid climate over Northwest China detected from A-Train satellite measurements. Atmos Chem Phys 2010;10: 6863–72.

[43] Ackerman P, Toon OB. Absorption of visible radiation in atmosphere containing mixtures of absorbing and nonabsorbing particles. Appl Opt 1981;20:3661–8.